Available online at www.sciencedirect.com

ScienceDirect

Geochimica et Cosmochimica Acta 236 (2018) 230–239

Geochimica et Cosmochimica Acta

www.elsevier.com/locate/gca

The distribution and coordination of trace elements in *Krithe* ostracods and their implications for paleothermometry

Oscar Branson [a,*], Simon A.T. Redfern [a], Aurora C. Elmore [a,b], Elizabeth Read [a], Sergio Valencia [c], Henry Elderfield [a,1]

[a] *Department of Earth Sciences, University of Cambridge, Downing St, Cambridge CB2 3EQ, UK*
[b] *National Geographic Society, Washington, DC 20036, USA*
[c] *BESSY II, Albert-Einstein-Str. 15, 12489 Berlin, Germany*

Received 9 February 2017; accepted in revised form 2 December 2017; available online 11 December 2017

Abstract

The Mg and Sr content of ostracod valves have been used to reconstruct past temperature and salinity, and their stable isotopes have been used to reveal aspects of marine, lake and estuary hydrology. However, significant uncertainties surround ostracod calcification processes, the incorporation mechanisms of trace elements, and the sensitivity of proxy tracers to complex confounding factors. The valves of most ostracods are composed of micron-scale crystalline grains embedded in an organic matrix. The fine-scale geochemistry of these structures, and the nature of the influence of biological mineralisation processes on valve chemistry, remain poorly constrained. We have performed sub-micron resolution X-ray microscopy of a marine *Krithe* ostracod valve, and determined the chemical coordination of Mg, and the distribution of Mg, Na and S throughout the crystal-organic valve structure. These trace elements display systematic sub-micron-scale compositional variations within the mineral grains and inter-granular matrix of the valve ultrastructure. These patterns imply that *Krithe* biomineralisation processes significantly modulate trace element incorporation at the sub-micron scale. Thus *Krithe* chemical composition is likely to be decoupled to some extent from the water in which they calcified. Most importantly, Mg K-edge Near-Edge X-Ray Absorption Fine Structure (NEXAFS) spectra, and the coincidence of high-Mg regions with S-rich organic layers reveal that Mg is not primarily hosted in the calcite structure in the valve. Our results highlight the need to understand the processes that drive this fine-scale chemical heterogeneity and their influence on connections between the external environment and valve geochemistry, if ostracods are to be used as sources of paleoenvironmental proxies.

1. INTRODUCTION

Carbonate biominerals provide an unparalleled geochemical archive of Earth's climate, which has been instrumental in understanding climate cycles and feedbacks (Lea, 2014). The use and interpretation of paleoenvironmental proxies depends upon robust relationships between biomineral geochemistry and external environmental conditions. These relationships are based upon the physical and chemical processes governing the distribution and speciation of elements in seawater, and the incorporation of these elements into carbonate minerals, which predict connections between the environment and shell geochemistry that can be demonstrated in inorganic precipitation experiments (e.g. Mucci and Morse, 1983). However, biomineralisation processes often cause deviations from behavour predicted

* Corresponding author at: Research School of Earth Sciences, Australian National University, 142 Mills Rd, Acton ACT 2601, Australia.
E-mail address: oscar.branson@anu.edu.au (O. Branson).
[1] Deceased 19th April 2016.

https://doi.org/10.1016/j.gca.2017.12.005
0016-7037/

by inorganic experiments (Weiner and Dove, 2003), so these geochemical proxies must rely on empirical, species-specific calibrations to account for these discrepancies (e.g. Anand et al., 2003). The interpretation of paleoproxies includes the implicit assumption that the tracers are incorporated directly into the mineral structure. This assumption has been shown to be true for Mg and B in foraminifera (Branson et al., 2015, 2013; Yoshimura et al., 2015), and Mg in brachiopods (Cusack et al., 2008; Yoshimura et al., 2015), bivalves, and calcitic corals (Yoshimura et al., 2015). In contrast, Mg in aragonitic corals appears to be hosted in a disordered, non-crystalline, and likely organic phase (Finch, 2008). If a trace element is hosted within the mineral lattice, knowledge of inorganic mineral systems may be used to understand the physical factors affecting its incorporation and subsequent preservation. Conversely, if an element is hosted in an alternative mineral or organic phase, other factors may control the incorporation and preservation of the tracer, and paleoproxy records derived from it become harder to interpret.

The stable isotopic composition and trace element content of the bi-valved, calcitic carapace (outer shell) of marine, estuarine, and lacustrine ostracods have been developed and applied as paleoenvironmental tracers (Chivas et al., 1986a, 1986b, 1983; Cronin et al., 2005, 2000; De Deckker et al., 1988; De Deckker and Forester, 1988; Dwyer et al., 2002; Elmore et al., 2012; Gray et al., 2014; Horne et al., 2012; Wansard and Mezquita, 2001). The Mg/Ca and Sr/Ca of ostracod valves are used as paleotemperature and paleosalinity proxies (Chivas et al., 1986a, 1986b). However, variations in ostracod Mg/Ca and Sr/Ca often deviate from relationships established in both inorganic precipitates and other biominerals (Elmore et al., 2012; Ito et al., 2003; Ito and Forester, 2008). The likely cause of such discrepancies are the poorly understood mechanisms of ostracod calcification (Ito and Forester, 2008).

Crustaceans mineralise their cuticle via a series of complex steps, involving epidermal layers, chitinous frameworks, and organic-rich gel layers (Yamada et al., 2005). In many crustaceans, the main carbonate component of *in-vivo* cuticle is amorphous calcium carbonate (ACC; Becker et al., 2005; Raz et al., 2002). This may also be the case in ostracods, given observations of valve ultrastructure, which reveal granular carbonate structures enclosed within an organic framework (Jørgensen, 1970; Keyser and Walter, 2004; De Deckker, 2017) homologous to other crustaceans. The involvement of ACC in crystallisation is known to influence calcite trace element content in inorganic systems (Wang et al., 2009), and could alter the sensitivity of trace element uptake to environmental parameters, particularly given the observation of ACC formation via calcium phosphate precursors (Keyser and Walter, 2004). Given the complex ultrastructure of ostracod valves, trace elements may be incorporated directly into the mineral structure or the organic chitinous framework, or be excluded to interstitial microdomains between the mineral and organic components, or a mixture of all three. Each trace element incorporation pathway may exhibit a distinct response to external environmental variability, and would require a distinct interpretation of trace element paleoenvironmental proxies.

Here, we investigate the sub-micron scale distribution and coordination (chemical bonding environment) of S, Mg and Na within the carapace of a *Krithe* ostracod using an X-ray Photo-Emission Electron Microscope (XPEEM). The coordination and distribution of S allows us to map organic material within the *Krithe* carapace. The coordination and distribution of Mg reveals aspects of Mg incorporation that shed light on the utility of the ostracod Mg/Ca temperature proxy. Finally, while the function of Na in ostracod mineralisation is unknown, it offers the potential to examine the similarity of incorporation of different ions into the carapace by comparison to the distribution of Mg, allowing us to probe the cation-specificity of trace element incorporation into the carapace. Together, the distributions of these elements reveal the significant influence that *Krithe* biomineralisation processes exert on sub-micron-scale geochemistry.

2. METHODS

2.1. Sample preparation

Specimens of benthic marine *Krithe* ostracods were obtained from the top 5 cm of deep-sea sediment core KN166-14 11JPC from the Gardar Drift (2707 m water depth; Iceland Basin, NE Atlantic), well above the lysocline (~4000 m). The top of core KN166-14 11JPC was shown in a previous study to be of Late Holocene age (665 ± 5 Calendar years ago) using AMS ^{14}C dating (Elmore and Wright, 2011; Elmore et al., 2015). For our sample preparation, ~5 cc of sediment was washed through a 63 μm sieve using deionised water and then dried over night at 40 °C. An adult-stage Krithe carapace was identified under a binocular microscope from the >250 μm sediment fraction. The carapace was brushed clean to remove observable surficial particles and visually inspected to ensure good preservation (translucent, non-granular appearance). The environmental conditions that the carapace was formed in are not well constrained.

An individual carapace valve was mounted in degassed EpoFix resin, and the sample surface was polished to a colloidal silica finish (1–5 nm grains). Polished samples received a two-step carbon coating: protective windows were placed over the specimens, and a ~50 nm carbon coat was applied to the exposed resin surface, the windows were then removed and a 1–2 nm carbon coat was applied to coat the entire sample surface.

A specimen of the benthic foraminifera *Aphistegina lessonii*, obtained from a live stock culture at Cambridge University, was also prepared following the same method. This sample serves as a coordination reference for Mg, which has previously been determined to be in an octahedral coordination, substituted for Ca in the calcite structure (Branson et al., 2013).

Microfossil samples were mounted in proprietary holders, designed to secure the specimen and provide a conductive path across the sample surface, and analysed by XPEEM at beamline UE49 of the BESSY II synchrotron

(Berlin). Samples were pumped down to a high vacuum (10–9 mbar) over 24 hours prior to analysis.

2.2. Data collection and analysis

Two sets of data were collected during analysis: spectral image stacks and difference maps between on- and off-peak energies (background-corrected peak intensity map). Data were collected from the K-edges of Na (1070.8 eV) and Mg (1303.0 eV), and the $L_{2\text{-}3}$ edge of S (162.5–163.6 eV). These edges arise from the excitation of 1s and 2p shell electrons, respectively. Data were analysed using a proprietary set of macros written within IGOR Pro (Kronast, 2013).

During data collection, the entire field of view was illuminated with a monochromatic X-ray beam >50 μm in diameter. The XPEEM measured the secondary photoelectrons emitted from the sample surface released by the Auger effect across a range of specific incident beam energies to generate a Near Edge X-ray Absorption Fine Structure (NEXAFS) spectrum. The X-ray beam penetrated up to several hundred nm into the sample, but the measured signal originates from the upper 10 s of nm. The photoelectrons emitted from the sample surface were focused by a series of electron lenses onto a phosphor screen, and imaged by a 2D detector.

For NEXAFS spectral scans the range extended to approximately 15 eV below and 30 eV above the edge under consideration. During processing, multiple image stacks were collected, aligned and summed to maximise signal: noise. Spectra from each component scan were identical within signal:noise limits, demonstrating that beam damage effects were negligible. Spectra were extracted from specific regions within the specimen to examine spatial variations in element coordination, guided by an off-edge X-ray image. After extraction, spectra were imported into R (R Core Team, 2012; RStudio, 2013), where a linear background running through the first and last five points of each spectrum was subtracted, and each spectrum was normalised between zero and one by dividing by the peak maximum.

Difference maps were used to map peak intensities, by correcting on-peak images for non-element-specific emission and illumination inhomogeneities. Sets of 20 pre-edge, 40 on-edge and 20 pre-edge images of 2 s exposure each were collected, aligned, and summed in IGOR Pro. The summed on-edge images were then divided by the pre-edge images to provide the peak intensity maps. Prior to collection, a rough NEXAFS spectrum was obtained to confirm the positions of the emission peaks. Note that these on-peak images should more strictly be considered to represent a combination of elemental coordination state and concentration. However, for elements that show uniform coordination across the sample, these maps may be interpreted as representative of elemental concentration.

2.3. Cross-grain profiles

Chemical patterns within the granular structure of the carapace were quantified by cross-grain profiles. Profiles were extracted from map data along 5-pixel-wide lines using ImageJ (Schindelin et al., 2012), normalised between zero and one, and scaled by aligning the inflection points in the off-peak profile to account for differences in grain size.

2.4. Electron probe maps

Electron probe micro-analysis (EPMA) maps of the specimens were collected after XPEEM analyses using a modified technique after Sadekov and Eggins, 2005, employing a finer beam (~1 μm Θ), a smaller step size (0.5 μm), and a 1 s count time for all analytes.

2.5. Scanning electron microscopy

SEM images were taken using a Hitachi TM 3000 microscope in both normal imaging mode, and topographic imaging mode, which increases topographic contrast by comparing left- and right-illuminated images.

3. RESULTS

3.1. Broad-scale sample structure

SEM imaging revealed heterogeneities in electron density on the sample surface (Fig. 1B), consistent with a cross-sectional view of the crystal-organic matrix structure present within *Krithe* valves (De Deckker, 2017). These features do not correspond to sample topography, which was negligible on the scale of our analyses (Fig. 1B). EPMA maps of Mg/Ca and Na/Ca reveal that both elements are relatively homogeneous at the micron-scale (Fig. 1C), and certainly compared to the systematic chemical heterogeneity observed in other biominerals, including foraminiferal calcite (Branson et al., 2013; Sadekov and Eggins, 2005). There is some heterogeneity in both Mg and Na at the ~10 μm scale, with a ~5 μm wide band of elevated Mg and Na concentration running parallel to the outer valve surface, in rough agreement with a similar high Mg/Ca band observed in De Deckker's (2017) microprobe study (Fig. 1C). There is also a marked increase in Na and especially Mg in the muscle scar, which is likely to be enriched in organic material (Fig. 1C).

An XPEEM off-edge total electron yield (at an energy that does not correspond to a specific elemental absorption edge) image shows the electron density at the sample surface at sub-micron-scale resolution (Fig. 2). This reveals a distinctive 'granular' pattern, with lower-electron-density grains between 0.5–2 μm long embedded in a higher-density matrix, reminiscent of early ostracod TEM micrographs (Jørgensen, 1970), and again consistent with the crystal-organic matrix structure of the *Krithe* valve (De Deckker, 2017). Based on comparison to these previous ultrastructural obsercations, the 'bright' regions likely correspond to relatively electron-dense organic materials, and the 'dark' regions to relatively electron sparse crystalline material. The specimen surface is flat on the scale of these features, and therefore they are not artefacts of sample topography (Fig. 1B). Spectral data are presented from the entire sample ('total'), electron-dense ('bright') and electron-sparse ('dark') regions separately, to investigate

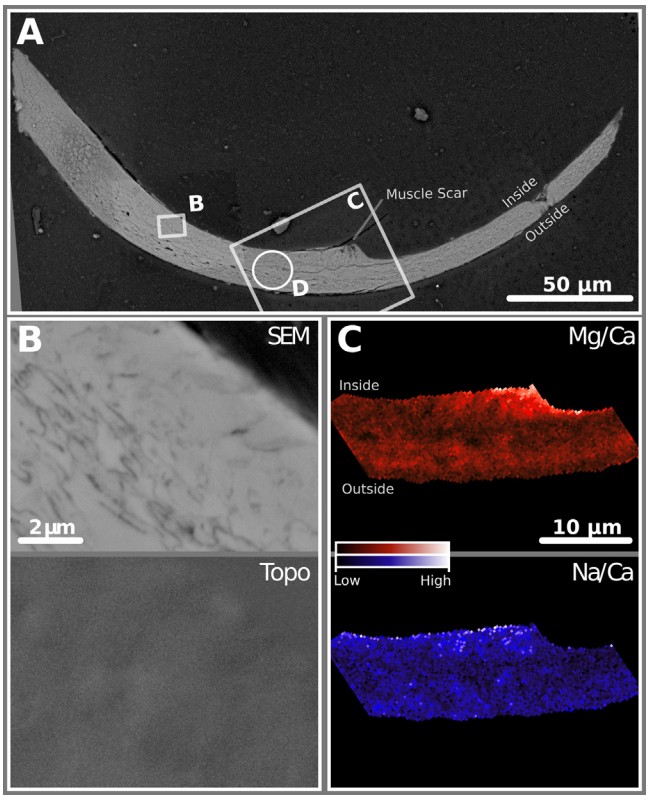

Fig. 1. (A) An SEM of the embedded, polished *Krithe* ostracod valve cross-section showing (B) a high magnification SEM of the sample surface and sample topography and (C) EPMA Mg and Na maps of the sample. Note the ~5 µm wide relatively Mg- and Na-enriched band toward the outer edge of the valve, and the significantly Mg- and Na-enriched region within the muscle scar, which is likely enriched in organic material. The topographic image (B: Topo) shows that the sample is flat on the scale of the chemical features observed in XPEEM maps. (D) Shows the approximate location of the area analysed by XPEEM.

the uniformity of element coordination between the whole valve, organic and crystalline regions, respectively.

3.2. Spectral results

The Mg spectra measured from foraminiferal calcite contains the same spectral features as those collected by previously-reported scanning transmission X-ray microscopy (STXM) NEXAFS techniques (Fig. 3) (Branson et al., 2013; Yoshimura et al., 2015). The energy resolution of the XPEEM is lower than the X-ray absorption or fluorescence techniques employed in our previous studies, but the similarity of our foraminiferal spectrum to previous results demonstrates that the XPEEM is able to resolve the coordination of calcite-bound trace elements of similar concentration to Mg in *A. lessonii*. The bulk Mg/Ca of *Krithe* is typically 8–17 mmol/mol (Elmore et al., 2012; Gray et al., 2014; Mewes et al., 2015), compared to 10–40 mmol/mol in *A. lessonii* (Branson et al., 2013). Any Mg spectra from *Krithe* may be up to 5x less intense than *A. lessonii*, but this comparison serves to demonstrate the accuracy of the Mg edge position in XPEEM, and the overall shape of calcite-hosted Mg spectra.

The Mg absorption edge in the ostracod specimen is broad, lacks distinct features. The absorption edge position, and the overall Mg spectra shape is dissimilar from the foraminiferal Mg spectrum (Fig. 3). The *Krithe* Mg spectrum also bears no clear similarity to any of the wide variety of previously measured spectra of Mg-bearing mineral phases (Branson et al., 2013; Cusack et al., 2008; Farges et al., 2009; Finch, 2008, 2007; Foster et al., 2008; Yoshimura et al., 2015), which tend to be characterised by well-defined peaks. The Mg spectra from 'bright' and 'dark' sample regions are of different intensities, but there are no consistent differences in their shape, indicating that while ultrastructural changes in the carapace correspond to changes in Mg concentration, there is no variation in Mg coordination.

As with the *Krithe* Mg spectrum, the S spectrum is broad, and lacks well-defined features (Fig. 4A). Two broad peaks at ~150 and ~160 eV appear to varying degrees in the ostracod S spectra. The ~160 eV peak is most intense in the 'bright' regions of the valve, and dominates the 'total' spectrum. This peak is consistent with the S $L_{2,3}$-edge, although the overall peak structure is distinct from previously published S spectra (Fleet, 2005; Kasrai et al., 1990; Pingitore et al., 1995). The ~150 eV peak dominates in the 'dark' regions, and is a minor component in the 'total' and 'bright' regions. This could imply a significant change in S coordination between the grains and the inter-grain matrix, although a 10 eV shift is large and improbable. Alternatively, the ~150 eV peak could be attributable to

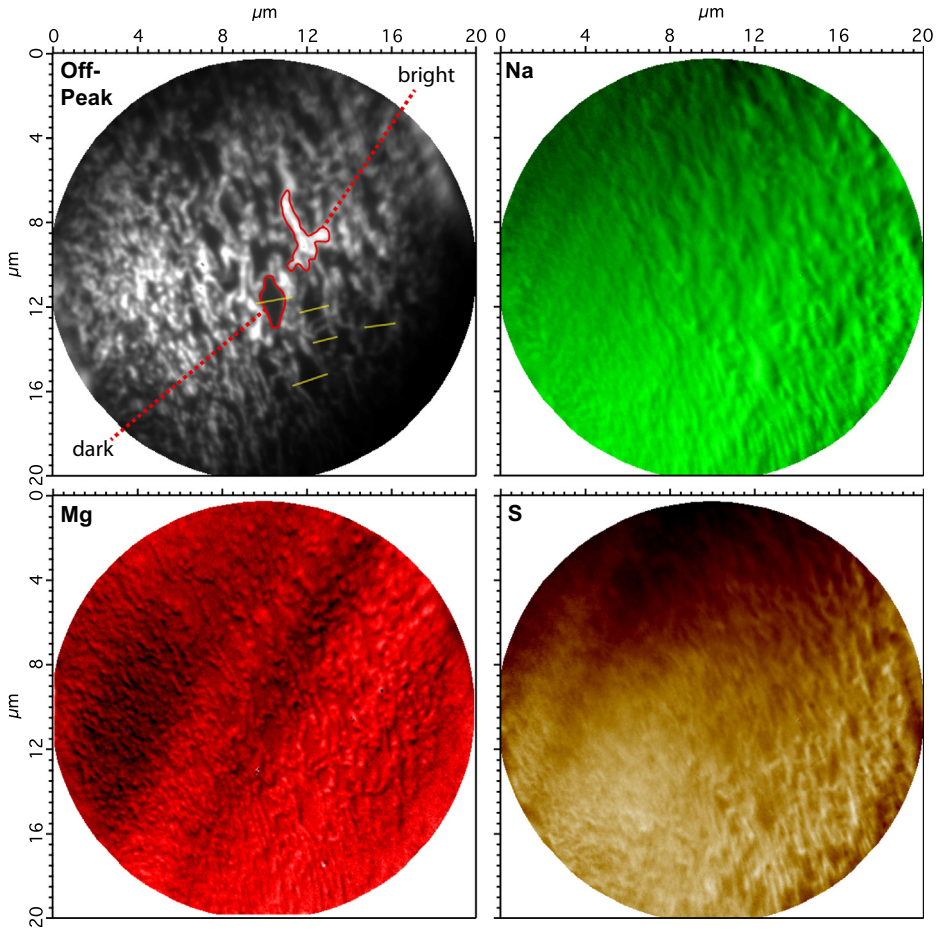

Fig. 2. XPEEM maps of electron-density (off-peak) and elemental peak intensity within the *Krithe* carapace. Darker colours indicate lower intensity, lighter colours indicate higher intensity in all images. The off-peak image reveals a granular electron-density pattern, with lower-density (dark) grains embedded within a higher-density (light) framework. Within this structural setting, both Na and Mg exhibit a 'topographic' appearance, with 'highlights' and 'shadows' on opposing sides of the dark granular structures. Na appears 'illuminated' from the lower left, while Mg is 'lit' from the upper right. The sample was flat at the scale of these features (Fig. 1B), so these features result from chemical heterogeneity, rather than sample illumination artefacts. S appears elevated in the inter-granular framework, most associated with sulphated organics. The systematic elemental heterogeneity in this granular framework is shown in detail in cross-grain profiles (Fig. 5) extracted from left to right along the yellow lines in the off-peak image. Red outlined regions denote the source of the 'bright' and 'dark' spectra in Figs. 4 and 5. The parallel, long-wavelength diagonal bright/dark banding features that are particularly evident in Mg and Na maps are analytical artefacts, and should not be interpreted. These features are parallel to the orientation of the X-Ray beam slits, and are attributable to up-stream beam variations during our long acquisition times. (For interpretation of the references to colour in this figure legend, the reader is referred to the web version of this article.)

the L_2-edge of Phosphorous (e.g. Yang et al., 2012), which would imply a concentration of P in the 'dark' (crystalline) region.

The *Krithe* Na spectrum is noisy because of the relatively low Na concentration, the low quantum yield of the Na K-edge, and limits on instrument count time. This precludes any conclusive identification of peaks within the data. However, smoothed spectra show a double-peaked structure at the Na edge (Fig. 4B), which bears no resemblance to any Na mineral spectra presently reported in the literature (De Wispelaere et al., 2004; Neuville et al., 2004; Yoshimura et al., 2017). Meaningful conclusions on the Na coordination state cannot be drawn on the basis of these spectra, but they do confirm the position of the Na K-edge in the ostracod specimen, allowing the creation of Na maps. As with the Mg spectrum, there are no significant Na spectral differences between 'bright' and 'dark' regions of the *Krithe* ultrastructure.

3.3. Elemental distribution

Absorption-edge maps of Mg, Na and S within the *Krithe* valve (Fig. 2) all show distinctive patterns that correspond to aspects of the granular ultrastructure seen in the off-peak electron density image. These patterns are highlighted in cross-grain chemical profiles (Fig. 5). Both Mg and Na exhibit systematic heterogeneity within the low-density grains. Mg is elevated on the upper right of each grain, and depleted on the lower left, while Na shows the opposite pattern (Figs. 2 and 3). Maximum Mg intensities

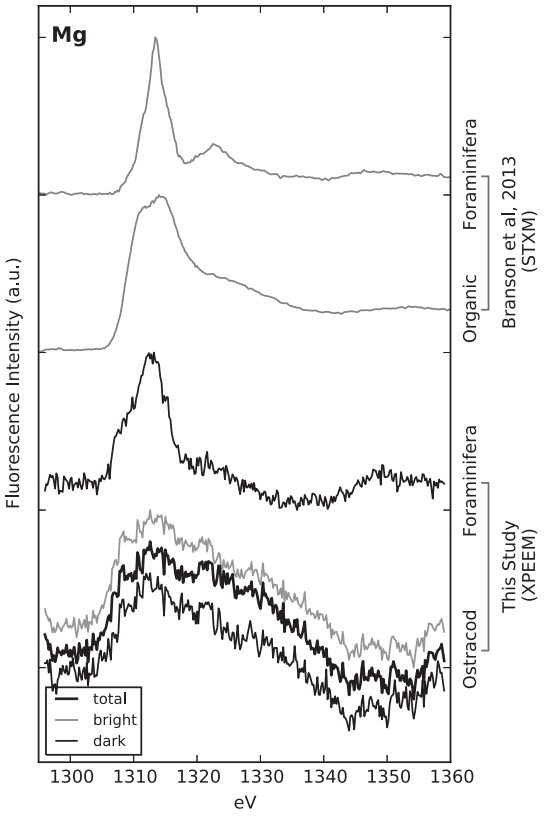

Fig. 3. Normalised Mg K-edge NEXAFS spectra from the reference foraminifera *A. lessonii*, organic material, and our *Krithe* ostracod specimen. The top two spectra were measured by STXM, reproduced from Branson et al. (2013). The bottom spectra are from our XPEEM study. The foraminiferal spectrum is notably broader in the XPEEM data, with a less structured post-edge region than that of the previously published STXM method. The *Krithe* Mg spectrum is much broader than the foraminiferal Mg spectrum measured by either method, or the organic spectrum, and has a lower energy Mg edge. Spectra from 'bright', 'dark' and 'total' regions of the ostracod valve are equivalent, within instrumental noise. Representative 'bright' and 'dark' regions are shown in Fig. 2. All spectra are normalised between zero and one, and are presented on an arbitrary, unitless scale.

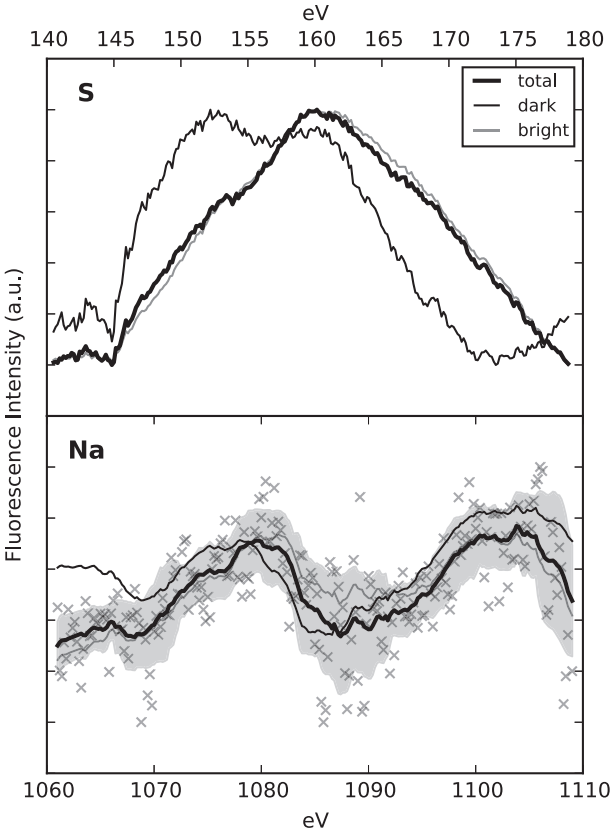

Fig.4. Normalised S $L_{2,3}$-edge and Na K-edge spectra from the *Krithe* valve. In the S spectra, the differences between electron-dense ('bright') and electron-sparse ('dark') regions, and the similarity between 'total' and 'bright' indicate that the majority of S is hosted in the 'bright' phase, with a smaller component hosted in the 'dark' phase, most likely calcite. The spectrum from the 'dark' phase is characterised by a strong peak at ~150 eV, which may be the P L_2-edge, rather than a shifted S edge. The Na spectra are displayed as a 3-point running mean, with an associated standard deviation envelope. There is no significant difference between 'bright' and 'dark' regions. Representative 'bright' and 'dark' regions are shown in Fig. 2. All spectra are normalised between zero and one, and are presented on an arbitrary, unitless scale.

are observed in the inter-grain matrix, while maximum Na is observed within lower right edges of the grains. In contrast, S appears relatively homogenous and depleted within the grain body, and is enriched in the inter-grain matrix. Note that these absorption-edge maps are sensitive to both changes in element concentration and coordination. Thus, Mg and Na maps may be interpreted as elemental concentration maps because of their spatially homogeneous spectra, while the S maps are complicated by possible coordination changes, evident in the variation of S spectra between 'bright' and 'dark' regions.

4. DISCUSSION

Our XPEEM analyses corroborate the well-documented organic-mineral composite valve ultrastructure observed in previous studies of ostracods (Jørgensen, 1970; Keyser and Walter, 2004; De Deckker, 2017), revealing a network of mineral grains hosted within an organic matrix. Our elemental maps show systematic patterns of element distribution and coordination within the crystal grains and inter-crystalline organic matrix, which are present throughout the region of the valve analysed. Combined with the ubiquity of this crystal-organic structure within *Krithe* valves (De Deckker, 2017), these systematic patterns are likely to be characteristic of these structural units, and present throughout the entire valve. Our observations show that biomineralisation processes exert a significant, systematic influence on the sub-micron-scale chemistry of the valve, but we cannot discern how changes in the external environment or ontogeny may influence these patterns. The specific magnitudes and nature of the patterns observed in this study may be unique to this specimen, and considerable further ultrastructural work is required to investigate

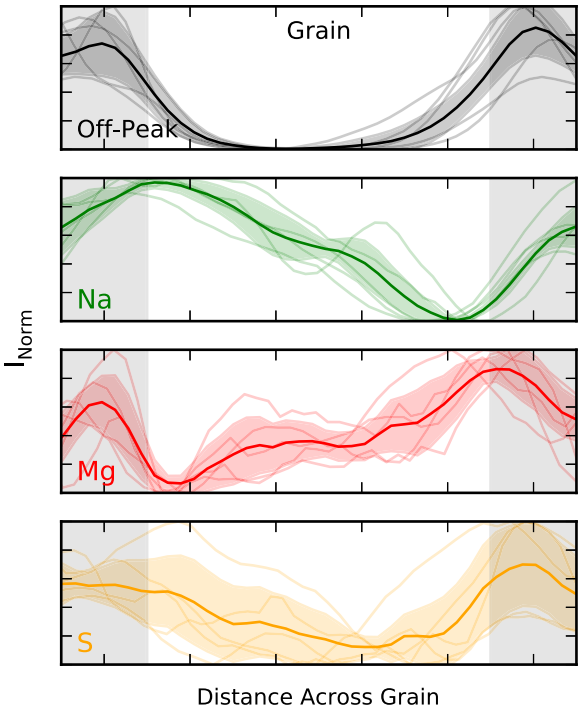

Fig. 5. Cross-granular profiles reveal systematic compositional patterns within the carapace structure. The grain body is within the white area in the centre of the profiles, and inter-granular framework is denoted by the grey regions on either side of the profiles. Within the grains, Na decreases and Mg increases from left to right, while S is more variable. Mg and S are both elevated within the inter-granular material, compared to the grain body. Na is most abundant within the grain body, on the left hand side. Thick lines and error envelope denote the mean and standard deviation of five profiles, extracted from the lines shown in Fig. 2. All profiles are normalised between zero and one, and are presented on an arbitrary, unitless scale.

the role of these fine-scale processes play in modulating links between bulk valve chemistry and the external environment, and their use as paleoproxy recorders. Nevertheless, our ultrastructural chemical data provide an opportunity to investigate the contribution of specific aspects of ostracod biomineralisation to valve chemistry.

The broad S-edge spectrum in *Krithe* is indicative of a relatively disordered coordination environment, most likely associated with organic molecules. The high concentration and distinct coordination state of S within the electron-dense ('bright'), inter-granular matrix may imply the presence of an interstitial sulphated organic molecule. For example, sulphated polysaccharides are common in numerous invertebrate calcareous structures, and are thought to play a role in facilitating ACC-mediated mineralization (Cuif et al., 2008), which is known to be important in ostracods (Keyser and Walter, 2004) and other crustaceans (Becker et al., 2005; Raz et al., 2002). The dominance of the ~150 eV peak in the crystal grain ('dark') spectra may indicate a concentration of P within the crystal grains, which is consistent with previous observations of calcium phosphate precursors in ostracod mineralisation (Keyser and Walter, 2004).

The lack of similarity between our *Krithe* Mg spectra and the spectra of calcite-hosted Mg (Fig. 3) (Branson et al., 2013; Cusack et al., 2008; Farges et al., 2009; Finch, 2008, 2007; Foster et al., 2008; Yoshimura et al., 2015) suggests that the bulk of the Mg in the ostracod carapace is unlikely to be substituted for Ca in the calcite mineral structure. While determination of precise Mg coordination is not possible from our spectra, the broad nature of the Mg-edge implies a highly variable coordination state, most similar to that of organic-associated Mg that has been measured in previous studies (Branson et al., 2013; Finch, 2008; Yoshimura et al., 2015). Alongside the relatively high abundance of Mg within the S-rich, electron-dense matrix, and the relatively high Mg content of the non-soluble organic matrix of ostracods (Chivas et al., 1983), this implies that a significant portion of total valve Mg is hosted within the inter-granular organic matrix. The similarity of the Mg spectra between electron-dense matrix and electron-sparse grains further implies that even Mg present in the crystalline component of the valve may be hosted within intra-crystalline organic components.

The homogeneity of Mg and Na spectra throughout the valve ultrastructure allow us to interpret their absorption-edge maps as indicative of elemental concentration, rather than coordination changes. The relative distributions of Mg and Na offer insights into the mineralisation of crystal grains in the carapace. Within each grain, Na is elevated on the lower left, and Mg is elevated on the upper right. Changes in concentration across a crystal grain may either be driven by changes in precipitation rate driving variations in the kinetic fractionation of trace elements, Rayleigh fractionation processes driving changes in fluid composition in a closed environment, or differences in the inclusion of intra-crystalline trace-element rich organic components. The anticorrelation of Mg and Na (Fig. 5) exclude Rayleigh fractionation as the source of the pattern in both elements, but could be explained by a change in crystal growth rate across the grain. However, given the likelihood that Mg is hosted within an organic phase, the increase in Mg content across the grain is may reflect changes in the concentration of a Mg-rich organic component within the grain. If this is the case, Na variability may either be attributable to a Rayeigh reservoir effect, or the change in concentration of a different type of organic component that is anti-correlated with Mg. Both Na and Mg have been observed to be specifically associated with biomineralisation-related organics in magnetite (Gordon and Joester, 2011) and carbonate (Branson et al., 2016) biominerals.

Our high-resolution XPEEM maps reveal the presence of sub-micron-scale elemental heterogeneity in *Krithe* at the single-crystal-grain level, rather than bisecting the underlying shell microstructure, as in foraminifera (Branson et al., 2013; de Nooijer et al., 2014; Sadekov and Eggins, 2005). Combined with the lack of clear evidence for a crystalline-hosted coordination environment for Mg, Na, or S within the ostracod carapace, this is indicative of a complex biomineralisation mechanism, whereby biological mechanisms actively control specific trace elements during carapace mineralisation. Such complexity has been previously reported from ultrastructural

observations (Jørgensen, 1970; Keyser and Walter, 2004; De Deckker, 2017), but the implications for carapace geochemistry have thus far remained unexplored.

Based on our observations, it is clear that the processes of ostracod biomineralisation exert a strong influence over carapace chemistry. Understanding these controls, and their sensitivity to the external environment and ontogeny, is crucial to their use as a source of geochemical proxy material. Most importantly, our *Krithe* data show that Mg is not predominantly hosted within the calcite mineral lattice. This suggests that thermodynamic controls need not define the relationship between temperature and ostracod Mg/Ca. This raises two significant areas of uncertainty, which must be addressed if ostracods are to continue to be used as a source of paleoceanographic proxies:

1. *The controls on Mg uptake into organic material*. In particular, the relation of Mg uptake to temperature, and other environmentally variable factors (e.g. food supply, growth rate, salinity). Because of its high Mg content, the processes controlling organic chemistry have the potential to dwarf any thermodynamically-driven mineral-hosted Mg/Ca signal.
2. *The influence of diagenesis on valve organic content and composition*. The preservation of organic material is unlikely to be similar to calcite. This raises significant issues for the down-core application of ostracod Mg/Ca paleothermometer, as the rates of change of the composition and abundance of organic and mineral material with time are unknown.

It is possible that estuarine and lacustrine ostracod species may incorporate Mg using distinct mechanisms from the benthic marine *Krithe* ostracod investigated here, and could have predominantly calcite-hosted Mg. However, given the Mg-rich organic present in non-marine ostracods (Chave, 1954), and the similar organic-mineral composite structure of numerous ostracod species (De Deckker, 2017), we consider this unlikely. Whilst we are unable to address the coordination of Sr in this experiment, our results raise significant questions surrounding the incorporation mechanisms of all trace elements in ostracods. These must be addressed before the they can be confidently used as a source of geochemical paleoceanographic proxy material.

5. CONCLUSIONS

Our results indicate that the incorporation of Mg, Na, and S in *Krithe* are significantly modulated by biomineralisation processes at the sub-micron scale, and is not comparable to inorganic calcite precipitation. Therefore, the assumptions that normally underpin our use of calcite-bound paleoproxies cannot be applied to ostracods. Significantly, we find that Mg is not predominantly hosted in the *Krithe* calcite mineral lattice, and is concentrated in the inter-granular organic material within the carapace, which raises significant questions surrounding the mechanisms behind the Mg/Ca ostracod paleothermometer. Importantly, while we have revealed biomineralisation-driven patterns in valve chemistry, the specific patterns observed in this specimen may vary with external environment, ontogeny, or between species. The role of these sub-micron-scale biomineralisation processes on modulating whole-valve geochemistry must be systematically evaluated, if their trace elements are to be used as a source of paleoproxy material.

ACKNOWLEDGEMENTS

The authors would like to thank Iris Buisman, Martin Walker, Giulio Lamproti, Richard Twitchett, John Spicer and James Wright for their help with obtaining, preparing and analysing samples. We would also like to thank Patrick De Deckker, for useful discussions about our results and interpretation, and three anonymous reviewers for their constructive comments. The work was funded by a beamtime proposal to the Bessy II synchrotron, NERC PhD studentships awarded to OB and ER, and by an ERC (2010-NEWLOG ADG-267931 grant to HE).

REFERENCES

Anand P., Elderfield H. and Conte M. (2003) Calibration of Mg/Ca thermometry in planktonic foraminifera from a sediment trap time series. *Paleoceanography* **18**, 28–31.

Becker A., Ziegler A. and Epple M. (2005) The mineral phase in the cuticles of two species of Crustacea consists of magnesium calcite, amorphous calcium carbonate, and amorphous calcium phosphate. *Dalton Trans.* **10**, 1814–1820.

Branson O., Kaczmarek K., Redfern S. A. T., Misra S., Langer G., Tyliszczak T., Bijma J. and Elderfield H. (2015) The coordination and distribution of B in foraminiferal calcite. *Earth Plan. Sci. Lett.* **416**, 67–72.

Branson O., Redfern S. A. T., Tyliszczak T., Sadekov A. Y., Langer G., Kimoto K. and Elderfield H. (2013) The coordination of Mg in foraminiferal calcite. *Earth Plan. Sci. Lett.* **383**, 134–141.

Branson O., Bonnin E. A., Perea D. E., Spero H. J., Zhu Z., Winters M., Hönisch B., Russell A. D., Fehrenbacher J. S. and Gagnon A. C. (2016) Nanometer-scale chemistry of a calcite biomineralisation template: implications for skeletal composition and nucleation. *Proc. Nat. Acad. Sci. USA* **113**, 12934–12939.

Chave K. E. (1954) Aspects of the biogeochemistry of magnesium 1. Calcareous marine organisms. *J. Geol.* **62**, 266–283.

Chivas A. R., de Deckker P. and Shelley J. M. G. (1986a) Magnesium and strontium in non-marine ostracod shells as indicators of paleosalinity and paleotemperature. *Hydrobiologia* **143**, 135–142.

Chivas A. R., de Deckker P. and Shelley J. M. G. (1986b) Magnesium content of non-marine ostracod shells: a new paleosalinometer and paleothermometer. *Paleogeog. Paleoclim. Paleoecol.* **54**, 43–61.

Chivas A. R., de Deckker P. and Shelley J. M. G. (1983) Magnesium, strontium, and barium partitioning in nonmarine ostracode shells and their use in paleoenvironmental reconstructions – a preliminary study. *Appl. Ostracoda*, 238–249.

Cronin T. M., Dowsett H. J., Dwyer G. S., Baker P. A. and Chandler M. A. (2005) Mid-pliocene deep-sea bottom-water temperatures based on ostracode Mg/Ca ratios. *Mar. Micropaleontol.* **54**, 249–261.

Cronin T. M., Dwyer G. S., Baker P. A., Rodriguez-Lazaro J. and DeMartino D. M. (2000) Orbital and suborbital variability in North Atlantic bottom water temperature obtained from deep-

sea ostracod Mg/Ca ratios. *Paleogeog. Paleoclim. Paleoecol.* **162**, 45–57.

Cuif J. P., Dauphin Y., Farre B., Nehrke G., Nouet J. and Salomé M. (2008) Distribution of sulphated polysaccharides within calcareous biominerals suggests a widely shared two-step crystallization process for the microstructural growth units. *Min. Mag.* **72**, 233–237.

Cusack M., Perez-Huerta A., Janousch M. and Finch A. A. (2008) Magnesium in the lattice of calcite-shelled brachiopods. *Chem. Geol.* **257**, 59–64.

De Deckker P. (2017) Trace elemental distribution in ostracod valves. From solution ICPMS and laser ablation ICPMS to microprobe mapping: a tribute to Rick Forester. *Hydrobiologia* **786**, 23–39.

De Deckker P., Chivas A. R., Shelley J. M. G. and Torgersen T. (1988) Ostracod shell chemistry: a new paleoenvironmental indicator applied to a regressive/transgressive record from the gulf of Carpentaria, Australia. *Paleogeog. Paleoclim. Paleoecol.* **66**, 231–241.

De Deckker P. and Forester R. M. (1988) The use of ostracods to reconstruct continental paleoenvironmental records. In *Ostracoda in the Earth Sciences* (eds. P. De Deckker, J. P. Colin and J. P. Peypouquet). Elsevier, Amsterdam, pp. 175–199.

De Nooijer L. J., Spero H. J., Erez J., Bijma J. and Reichart G. J. (2014) Biomineralization in perforate foraminifera. *Earth Sci. Rev.* **135**, 1–11.

De Wispelaere S., Cabaret D., Levelut C., Rossano S., Flank A.-M., Parent P. and Farges F. (2004) Na-, Al-, and Si K-edge XANES study of sodium silicate and sodium aluminosilicate glasses: influence of the glass surface. *Chem. Geol.* **213**, 63–70.

Dwyer G. S., Cronin T. M., Baker P. A. (2002) Trace elements in marine ostracodes. In The Ostracoda: Applications in Quaternary Research. American Geophysical Union, Washington, D. C.

Elmore A. C., Sosdian S., Rosenthal Y. and Wright J. D. (2012) A global evaluation of temperature and carbonate ion control on Mg/Ca ratios of ostracoda genus Krithe. *Geochem. Geophys. Geosyst.* **13**, Q09003.

Elmore A. C. and Wright J. D. (2011) North Atlantic Deep Water and climate variability during the Younger Dryas cold period. *Geology* **39**, 107–110.

Elmore A. C., Wright J. D. and Southon J. (2015) Continued meltwater influence on North Atlantic Deep Water instabilities during the early Holocene. *Mar. Geol.* **360**, 17–24.

Farges F., Meibom A., Flank A., Lagarde P., Janousch M. and Stolarski J. (2009) Speciation of Mg in biogenic calcium carbonates. *J. Phys.: Conf. Ser.* **190**, 012175.

Finch A. A. (2008) Mg structural state in coral aragonite and implications for the paleoenvironmental proxy. *Geophys. Res. Let.* **35**, L08704.

Finch A. A. (2007) Coordination of Sr and Mg in calcite and aragonite. *Min. Mag.* **71**, 539–552.

Fleet M. (2005) Xanes spectroscopy of sulfur in earth materials. *Can. Mineral.* **48**, 1811–1838.

Foster L., Finch A. A., Andersson C. and Clarke L. (2008) Mg in aragonitic bivalve shells: seasonal variations and mode of incorporation in Arctica islandica. *Geochem. Geophys. Geosyst.* **254**, 113–119.

Gordon L. M. and Joester D. (2011) Nanoscale chemical tomography of buried organic-inorganic interfaces in the chiton tooth. *Nature* **469**, 194–198.

Gray W., Holmes J. and Shevenell A. (2014) Evaluation of foraminiferal trace element cleaning protocols on the Mg/Ca of marine ostracod genus Krithe. *Chem. Geol.* **382**, 14–23.

Horne D., Holmes J., Viehberg F. and Rodriguez-Lazaro J. (2012) *Ostracoda as proxies for Quaternary climate change*. Elsevier Science.

Ito E., de Deckker P. and Eggins S. M. (2003) Ostracodes and their shell chemistry: implications for paleohydrologic and paleoclimatologic applications. *Paleontol. Soc. Pap.* **9**, 119.

Ito E. and Forester R. M. (2008) Changes in continental ostracode shell chemistry; uncertainty of cause. *Hydrobiologia* **620**, 1–15.

Jørgensen N. O. (1970) Ultrastructure of some ostracods. *Bull. Geol. Soc. Denmark* **20**, 79–92.

Kasrai M., Brown J. R., Bancroft G. M., Tan K. H. and Chen J. M. (1990) Characterization of sulphur in coal from sulphur L-edge XANES spectra. *Fuel* **69**, 411–414.

Keyser D. and Walter R. (2004) Calcification in ostracodes. *Evista Española de Micropaleontología* **36**, 1–11.

Kronast F. (2013) Igor Pro PEEM Macros.

Lea D. W. (2014) Elemental and isotopic proxies of past ocean temperatures. In Treatise on Geochemistry, Second Edition, vol. 8 (eds. H. D. Holland and K. K. Turekian). Elsevier, Oxford. pp. 373–397.

Mewes A., Langer G., Thoms S., Nehrke G. and Reichart G. J. (2015) Impact of seawater [Ca^{2+}] on the calcification and calcite Mg/Ca of *Amphistegina lessonii*. *Biogeosciences* **12**, 2153–2162.

Mucci A. and Morse W. (1983) The incorporation of Mg^{2+} and Sr^{2+} into calcite over- growths: influences of growth rate and solution composition. *Geochim. Cosmochim. Acta* **47**, 217–233.

Neuville D. R., Cormier L., Flank A.-M., Prado R. J. and Lagarde P. (2004) Na K-edge XANES spectra of minerals and glasses. *Eur. J. Mineral.* **16**, 809–816.

Pingitore N. E., Meitzner G. and Love K. M. (1995) Identification of sulfate in natural carbonates by x-ray absorption spectroscopy. *Geochim. Cosmochim. Acta* **59**, 2477–2483.

R Core Team (2012) *R: A Language and Environment for Statistical Computing*. R Foundation for Statistical Computing, Vienna, Austria.

Raz S., Testeniere O., Hecker A., Weiner S. and Luquet G. (2002) Stable amorphous calcium carbonate is the main component of the calcium storage structures of the crustacean *Orchestia cavimana*. *Biol. Bull.* **203**, 269–274.

RStudio (2013) RStudio: integrated development environment for R. Version 0.96.330.

Sadekov A. Y. and Eggins S. M. (2005) Characterization of Mg/Ca distributions in planktonic foraminifera species by electron microprobe mapping. *Geochem. Geophys. Geosyst.* **6**, L08704.

Schindelin J., Arganda-Carreras I., Frise E., Kaynig V., Longair M., Pietzsch T., Preibisch S., Rueden C., Saalfeld S., Schmid B., Tinevez J.-Y., White D. J., Hartenstein V., Eliceiri K., Tomancak P. and Cardona A. (2012) Fiji: an open-source platform for biological-image analysis. *Nat. Methods* **9**, 676–682.

Wang D., Wallace A., de Yoreo J. and Dove P. (2009) Carboxylated molecules regulate magnesium content of amorphous calcium carbonates during calcification. *Proc. Nat. Acad. Sci. USA* **106**, 21511–21516.

Wansard G. and Mezquita F. (2001) The response of ostracod shell chemistry to seasonal change in a Mediterranean freshwater spring environment. *J. Paleolimnol.* **25**, 9–16.

Weiner S. and Dove P. (2003) An overview of biomineralization processes and the problem of the vital effect. *Rev. Min. Geochem.* **54**, 1.

Yamada S., Tsukagoshi A. and Ikeya N. (2005) Carapace formation of the podocopid ostracode *Semicytherura* species (Crustacea: Ostracoda). *SLET* **38**, 323–332.

Yang S., Wang D., Liang G., Yiu Y. M., Wang J., Liu X., Sun X. and Sham T.-K. (2012) Soft X-ray XANES studies of various

phases related to $LiFePO_4$ based cathode materials. *Energy Environ. Sci.* **5**, 7007–7016.

Yoshimura T., Tamenori Y., Takahashi O., Nguyen L. T., Hasegawa H., Iwasaki N., Kuroyanagi A., Suzuki A. and Kawahata H. (2015) Mg coordination in biogenic carbonates constrained by theoretical and experimental XANES. *Earth Plan. Sci. Lett.* **421**, 68–74.

Yoshimura T., Tamenori Y., Suzuki A., Kawahata H., Iwasaki N., Hasegawa H., Nguyen L. T., Kuroyanagi A., Yamazaki T., Kuroda J. and Ohkouchi N. (2017) Altervalent substitution of sodium for calcium in biogenic calcite and aragonite. *Geochim. Cosmochim. Acta* **202**, 21–38. https://doi.org/10.1016/j.gca.2016.12.003.

Associate editor: Thomas M. Marchitto